



HAL
open science

A regime diagram for the slurry F-layer at the base of Earth's outer core

Jenny Wong, Christopher J. Davies, Christopher A. Jones

► **To cite this version:**

Jenny Wong, Christopher J. Davies, Christopher A. Jones. A regime diagram for the slurry F-layer at the base of Earth's outer core. *Earth and Planetary Science Letters*, 2021, 560, 10.1016/j.epsl.2021.116791 . insu-03590075

HAL Id: insu-03590075

<https://insu.hal.science/insu-03590075>

Submitted on 13 Feb 2023

HAL is a multi-disciplinary open access archive for the deposit and dissemination of scientific research documents, whether they are published or not. The documents may come from teaching and research institutions in France or abroad, or from public or private research centers.

L'archive ouverte pluridisciplinaire **HAL**, est destinée au dépôt et à la diffusion de documents scientifiques de niveau recherche, publiés ou non, émanant des établissements d'enseignement et de recherche français ou étrangers, des laboratoires publics ou privés.



Distributed under a Creative Commons Attribution - NonCommercial 4.0 International License

A regime diagram for the slurry F-layer at the base of Earth's outer core

Jenny Wong^{a,b,*}, Christopher J. Davies^c, Christopher A. Jones^d

^a*Université de Paris, Institut de physique du globe de Paris, CNRS, F-75005 Paris, France*

^b*EPSRC Centre for Doctoral Training in Fluid Dynamics, University of Leeds, Leeds, LS2 9JT, UK*

^c*School of Earth and Environment, University of Leeds, Leeds, LS2 9JT, UK*

^d*School of Mathematics, University of Leeds, Leeds, LS2 9JT, UK*

Abstract

Seismic observations of a slowdown in P wave velocity at the base of Earth's outer core suggest the presence of a stably-stratified region known as the F-layer. This raises an important question: how can light elements that drive the geodynamo pass through the stably-stratified layer without disturbing it? We consider the F-layer as a slurry containing solid particles dispersed within the liquid iron alloy that sink under gravity towards the inner core. We present a regime diagram showing how the dynamics of the slurry F-layer change upon varying the key parameters: Péclet number (Pe), the ratio between advection and chemical diffusion; Stefan number (St), the ratio between sensible and latent heat; and Lewis number (Le), the ratio between thermal and chemical diffusivity. We obtain four regimes corresponding to stable, partially stable, unstable and no slurries. No slurry is found when the heat flow at the base of the layer exceeds the heat flow at the top, while a stably-stratified slurry arises when advection overcomes thermal diffusion ($Pe \gtrsim Le$) that exists over a wide range of parameters relevant to the Earth's core. Our results estimate that a stably-stratified F-layer gives a maximum inner-core boundary (ICB) body

*Corresponding author

Email address: wong@ipgp.fr (Jenny Wong)

wave density jump of $\Delta\rho_{\text{bod}} \leq 534 \text{ kgm}^{-3}$ which is compatible with the lower end of the seismic observations where $280 \leq \Delta\rho_{\text{bod}} \leq 1,100 \text{ kgm}^{-3}$ is reported in the literature. With high thermal conductivity the model predicts an inner core age between 0.6 and 1.2 Ga, which is consistent with other core evolution models. Our results suggest that a slurry model with high core conductivity predicts geophysical properties of the F-layer and core that are consistent with independent seismic and geodynamic calculations.

Keywords: slurry, iron snow, inner core, crystallisation, F-layer

1 1. Introduction

2 Seismic, geomagnetic and dynamical explanations for and against the pres-
3 ence of stably-stratified layers in the Earth’s liquid core is an active research
4 topic of significant geophysical interest. Confirmation of their existence would
5 warrant a shift away from the usual approximation that the core is adiabatically
6 stratified with thin boundary layers. Stably-stratified layers should exhibit dy-
7 namics that distinguish them from the turbulent bulk of the core; elucidating
8 this behaviour will help to uncover their signature in seismic and geomagnetic
9 observations [1]. In this paper we focus on the F-layer at the base of the liq-
10 uid core to further understand the conditions where stable stratification can be
11 sustained.

12 There is a strong consensus that a slowdown in the P wave velocity compared
13 with the Preliminary Reference Earth Model (PREM) [2] is observed at the
14 base of the Earth’s outer core [3, 4, 5]. PREM follows the Adams-Williamson
15 equation that assumes the outer core is adiabatically stratified and homogeneous
16 throughout, therefore a P wave velocity lower than PREM is attributed to an
17 anomalously higher density structure than expected. This departure in density
18 away from neutral stability means that the seismic observations suggest a stably-
19 stratified layer exists that cannot be explained by adiabatic compression alone.

20 Estimates of the layer thickness vary from 150 km [3] to 400 km [4] thick, which
21 greatly exceeds the thermal diffusion length scale, hence the layer cannot be
22 simply explained by a thermal boundary layer alone and another mechanism is
23 required to maintain stratification [6].

24 The F-layer is intimately linked to the geodynamo process that generates
25 Earth's magnetic field. Motion of the liquid iron core is powered by heat ex-
26 tracted at the core-mantle boundary (CMB), which leads to freezing of the solid
27 inner core from the centre of the Earth because the melting curve is steeper than
28 the core adiabat. Freezing releases latent heat and light elements into the liquid;
29 light elements drive compositional convection in the core and is thought to be
30 the main power source for the dynamo at the present day [7]. The key issue
31 is buoyant light material excluded from the inner core must pass through the
32 F-layer and into the overlying core while preserving stable stratification.

33 Previous geodynamic models try to explain the F-layer by inner core transla-
34 tion [8], a thermochemical layer [9], or a slurry (iron snow) layer [10, 11]. Inner
35 core translation supposes melting occurs on the eastern hemisphere of the in-
36 ner core while freezing occurs on the western hemisphere to form a dense layer
37 above the inner-core boundary (ICB), though recent upward revisions of the
38 thermal conductivity of iron [12, 13] together with the likely presence of compo-
39 sitionally stabilising conditions suggest that the instability cannot arise in the
40 present-day [14, 15]. [9] proposed a thermochemical model with the F-layer on
41 the liquidus that succeeded in producing a stably-stratified layer, however, the
42 model effectively imposed a stable composition without a physical mechanism
43 explaining why. Wong *et al.* [11] explains this mechanism in a self-consistent
44 way by proposing a slurry layer that captures the physics of how light element
45 and solid is transported. The authors used a simple box model to demonstrate
46 that a slurry layer produced stably-stratified layers that match the seismic ob-

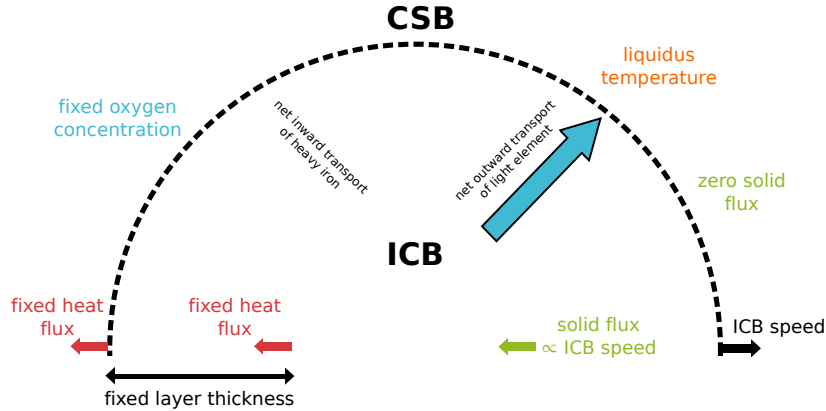


Figure 1: A sketch of the slurry layer at the base of Earth’s outer core, with the boundary conditions imposed at the inner core boundary (ICB) and core slurry boundary (CSB) described in Section 2.

47 servations of density and layer thickness. In this work we focus on the slurry
 48 scenario and build upon Wong *et al.* [11], hereafter referred to as W18.

49 In the slurry, pure solid iron particles crystallise throughout the entire F-
 50 layer while light elements remain in the liquid (see Figure 1 for a sketch). Heavy
 51 grains of iron fall under gravity to accumulate at the base of the layer, thereby
 52 producing a net inward transport of dense solid and a net outward transport
 53 of light elements to give an overall stable density stratification. W18 simplified
 54 the full slurry theory by Loper and Roberts [10, 16] and developed a reduced,
 55 thermodynamically self-consistent framework that accounts for solid and liquid
 56 phase, in addition to the influence of pressure, temperature and composition.
 57 The fraction of solid in a slurry is assumed to be small, and so cannot transmit
 58 shear waves to create an impedance contrast at the top of the F-layer that would
 59 otherwise have been seismically observable.

60 The principal assumptions of the W18 slurry model are (1) the fast-melting
 61 limit and (2) a binary alloy. (1) supposes that an infinitesimal material volume
 62 contains either solid or liquid phase exclusively so that the system is in phase

63 equilibrium. As a consequence, minimising the Gibbs free energy constrains the
64 slurry temperature to the liquidus. (2) presumes an Fe-O composition since
65 oxygen is able to explain the core density deficit [17]. *Ab initio* calculations
66 show that oxygen almost entirely partitions into the liquid phase upon freezing
67 [18] and cannot occur with silicon (another potential light element candidate) in
68 large quantities [19]. The solid produced by the slurry is thereby assumed to be
69 composed of pure iron, which avoids a complicated particle history dependence
70 that would be difficult to model, where the growth of solid grains at different
71 pressure-temperature conditions affects the composition of light elements in the
72 solid.

73 We generalise the W18 model by moving from a Cartesian to spherical ge-
74 ometry and update the boundary conditions to a more geophysically realistic
75 setup. We suppose that the inner core is isothermal and not convecting due to
76 the upward revisions of the thermal conductivity [20, 21] of iron alloys at core
77 conditions, which means that the present-day inner core is unlikely to convect.
78 We consider a thin compacting layer on the order of kilometres thick on the
79 solid side of the inner core [22], parameterised by interfacial freezing at the ICB
80 which generates a flux of latent heat into the slurry. Accordingly, the ICB ad-
81 vances at a rate composed of the interfacial freezing speed and the snow speed
82 given by the accumulation of solid iron particles from the slurry. Our model
83 self-consistently determines the ICB speed and therefore allows the inner core
84 growth rate to be independently determined, whereas this was fixed in W18 and
85 yielded unrealistically high ICB heat flows. Following the fast-melting limit, we
86 set the temperature at the top of the layer to the liquidus temperature for the
87 bulk core composition obtained from the literature, so that the ICB temperature
88 is free to be self-determined by the slurry whereas this was fixed in W18.

89 In this paper, we perform a systematic parameter search to elucidate the

90 conditions that promote stable stratification of the F-layer. The generalised
 91 model of W18 and the derivation of the dimensionless system with its associated
 92 dimensionless control parameters is given in Section 2. In Section 3, we present
 93 and discuss example solutions of the temperature, oxygen concentration, solid
 94 flux and density given by the slurry model with different layer thicknesses. We
 95 proceed to test the sensitivity of the model to the boundary conditions on the
 96 temperature and composition at the top of the layer, before mapping a regime
 97 diagram of the slurry based on the main dimensionless control parameters. This
 98 vastly improves upon the computed solution space of W18 and uncovers the
 99 possible regimes occupied by the slurry. We demonstrate the predictive power
 100 of our model for seismic observations and inner core age, before concluding with
 101 a summary of our findings in Section 4.

102 2. Model and Methods

103 2.1. Dimensional equations

104 Detailed development of the slurry model is given W18 so here we present
 105 the key details. We start with the general equations for the conservation of
 106 oxygen, temperature and the liquidus constraint from W18 (equations (4),(6)
 107 and (13)), given by

$$\rho^{sl} \frac{D\xi}{Dt} = -\nabla \cdot \mathbf{i}, \quad (1)$$

$$\rho^{sl} c_p \frac{DT}{Dt} = \nabla \cdot (k \nabla T + L \mathbf{j}) + \rho^{sl} L \frac{D\phi}{Dt}, \quad (2)$$

$$\nabla T = \frac{T \Delta V_{Fe}^{s,l}}{L} \nabla p - \frac{T \xi^l (\partial \mu / \partial \xi^l)}{L} \nabla \xi^l, \quad (3)$$

108 where p is the pressure, T is the temperature, ξ is the oxygen concentration,
 109 ξ^l is the oxygen concentration in the liquid phase, ϕ is the solid fraction, ρ^{sl} is
 110 the reference density of the slurry taken to be the PREM value at the CSB, \mathbf{i}

111 is the oxygen flux vector, \mathbf{j} is the solid flux vector, c_p is the specific heat ca-
 112 pacity, k is the thermal conductivity, L is the latent heat of fusion, $\Delta V_{Fe}^{s,l}$ is
 113 the change in specific volume between liquid iron and solid iron, and $\partial\mu/\partial\xi^l$
 114 is the thermodynamic derivative of the chemical potential, μ , with respect to
 115 ξ^l . Throughout this paper superscripts s , l and sl denote solid, liquid or slurry
 116 phases respectively, and subscripts Fe and O denote the iron and oxygen com-
 117 ponents, respectively. For further reference, a table of symbols and values is
 118 provided in Appendix A, Table A.2.

119 We adopt a spherical, one-dimensional geometry where we assume a global F-
 120 layer in a non-convective steady state that depends on radius only and excludes
 121 lateral variations. The layer thickness, d , is fixed so that the slurry is defined
 122 over the interval $[r^i, r^{sl}]$, where r^i denotes the ICB radius and $r^{sl} \equiv r^i + d$ is
 123 the core-slurry boundary (CSB). We are interested in a timescale that is long
 124 compared with the timescale of freezing and comparable to the evolution of
 125 the inner core [23], so we assume a Boussinesq slurry with a reference state in
 126 hydrostatic equilibrium, and resolve the slurry layer in a frame moving at the
 127 rate of inner core growth, $v\hat{\mathbf{f}}$, with v the ICB speed and $\hat{\mathbf{f}}$ the unit vector pointing
 128 outwards and normal to the inner core surface. Mass conservation $\nabla \cdot \mathbf{v} = 0$
 129 implies that $v(r) = v^i(r^i/r)^2$, where the changes in ICB speed due to radius are
 130 negligible and we therefore assume that v is constant. This speed is composed
 131 of two parts, $v = v_s + v_f$, where v_s is the snow speed, in which all solid particles
 132 from the slurry are assumed to accumulate at the base of the layer; and v_f is the
 133 freezing speed, which represents the growth of the inner core due to compaction
 134 on the solid side of the ICB, and assumed to occur quickly compared with the
 135 slurry timescale. The material derivative is hence $D/Dt \rightarrow -v d/dr$. As in
 136 W18, the fraction of solid, ϕ , in the slurry is small so that $\phi \ll 1$, and we
 137 assume that their variations, $d\phi$, are negligible (see discussion in Appendix B).

138 We apply the above assumptions to equations (1 – 3), to obtain,

$$-v\rho^{sl}\frac{d\xi^l}{dr} = \frac{1}{r^2}\frac{d}{dr}\left(r^2\frac{\rho^{sl}\Delta V_{Fe,O}^{s,l}D_O}{RT\frac{1000}{a_O}}\exp\left(\frac{F(r-r^i)}{d}\right)\frac{dp}{dr}\right) + \xi^l\frac{dj}{dr} + j\frac{d\xi^l}{dr} + \frac{2}{r}\xi^lj, \quad (4)$$

$$-v\rho^{sl}c_p\frac{dT}{dr} = k\frac{d^2T}{dr^2} + \frac{2}{r}k\frac{dT}{dr} + L\frac{dj}{dr} + \frac{2}{r}Lj, \quad (5)$$

$$\frac{dT}{dr} = -\frac{T\Delta V_{Fe}^{s,l}}{L}g\rho - \frac{RT^21000}{a_O L}\frac{d\xi^l}{dr}. \quad (6)$$

139 On the LHS of (4), we have the advection of oxygen, and on the RHS, the
 140 first term is the effect of barodiffusion and the last three terms describe the
 141 physical displacement of oxygen as solid iron particles sediment. On the LHS
 142 of (5), we have the advection of heat, and on the RHS, the first two terms
 143 correspond to thermal diffusion and the last two terms correspond to the latent
 144 heat release associated with phase change. The liquidus constraint (6) describes
 145 the change in the liquidus temperature as a consequence of changes in pressure,
 146 given by the first term on the RHS, and changes in composition, given by the
 147 second term on the RHS.

148 We have applied ideal solution theory [24] so that the thermodynamic deriva-
 149 tive of the chemical potential with respect to ξ^l can be expressed as $\xi^l\partial\mu/\partial\xi^l =$
 150 $RT1000/a_O$, where R is the gas constant and a_O is the atomic weight of oxy-
 151 gen. We expect penetrative convection to occur at the top of the layer because
 152 of the velocity difference between the non-convective slurry and the overlying
 153 convective outer core. We have thus invoked a turbulent mixing sublayer below
 154 the CSB that promotes the transport of oxygen out of the layer and also allows
 155 us to impose a vanishing solid flux boundary condition at the CSB (see equation
 156 (10) below). This effect is modelled by modifying the self-diffusion coefficient

157 of oxygen to take the exponential form

$$\bar{D} = D_O \exp\left(\frac{F(r - r^i)}{d}\right), \quad (7)$$

158 where F is the mixing parameter that appears in the first term on the RHS of
159 (4), and D_O is the self-diffusion coefficient of oxygen taken from the literature
160 [25].

161 2.2. Boundary conditions

162 We have three equations (4),(5), and (6) for three output variables T, ξ^l, j ,
163 and two output parameters (eigenvalues) F and v . The system is fourth order,
164 therefore we require six boundary conditions to determine a unique solution.
165 We suppose that the oxygen concentration is constant at the CSB and equal
166 to the uniform value in the bulk of the core, ξ^{sl} , since the liquid core is vigor-
167 ously convecting and its composition does not change much over the timescales
168 considered [26], so that

$$\xi^l(r^{sl}) = \xi^{sl}. \quad (8)$$

169 At the ICB the solid flux is proportional to the ICB speed and at the CSB the
170 solid flux vanishes, so that

$$j(r^i) = -\rho_-^s v, \quad (9)$$

$$j(r^{sl}) = 0, \quad (10)$$

171 where ρ_-^s denotes the density on the solid side of the ICB.

172 We fix the heat flux per unit area at the CSB to a constant value, q^{sl} , and
173 this is a parameter to be varied since there are no independent estimates. By

174 Fourier's law, the boundary condition on the CSB temperature gradient is

$$\frac{dT}{dr} \Big|_{r=r^{sl}} = -\frac{q^{sl}}{k}. \quad (11)$$

175 In the following two boundary conditions, we digress from the conditions im-
 176 posed in W18. First, compaction below the F-layer releases latent heat at
 177 the interface while there is no specific heat contribution from an isothermal IC,
 178 whereas W18 assumed specific heat loss from the inner core. Second, we assume
 179 that the temperature at the top of the layer is coincident with the liquidus tem-
 180 perature of the bulk composition, $T^{sl}(r^{sl})$, known from estimates given in the
 181 literature [25, 27], so that

$$\frac{dT}{dr} \Big|_{r=r^i} = -\frac{\rho^s v_f L}{k} = -\frac{q^s}{k}, \quad (12)$$

$$T(r^{sl}) = T^{sl}(r^{sl}). \quad (13)$$

182 where q^s is the ICB heat flux per unit area.

183 2.3. Dimensionless equations

184 We derive the dimensionless equations using the following scalings,

$$\begin{aligned} r &= r^{sl} \hat{r}, & T &= \frac{q^{sl}}{\rho^{sl} c_p v_f} \hat{T}, \\ \xi^l &= \xi^{sl} \hat{\xi}, & j &= \rho^s v_f \hat{j}, \\ g &= g^{sl} \hat{g}, & \rho &= \rho^{sl} \hat{\rho}, \\ v &= v_f \hat{v} \end{aligned} \quad (14)$$

185 where the hat symbol denotes a dimensionless quantity that depends on radius.
 186 The slurry layer is defined over the dimensionless interval $[r^i/r^{sl}, 1]$. Equations

187 (4)–(6) respectively become

$$-\hat{v} \frac{d\hat{\xi}}{d\hat{r}} = -\frac{1}{\hat{r}^2} \frac{d}{d\hat{r}} \left(\frac{Li_p R_\rho}{Li_\xi Pe St R_v} \frac{\hat{g} \hat{\rho} \hat{r}^2}{\hat{T}} \exp \left[\frac{F(r^{sl} \hat{r} - r^i)}{d} \right] \right) + \hat{\xi} \frac{d\hat{j}}{d\hat{r}} + \hat{j} \frac{d\hat{\xi}}{d\hat{r}} + \frac{2}{\hat{r}} \hat{\xi} \hat{j}, \quad (15)$$

$$-\hat{v} \frac{d\hat{T}}{d\hat{r}} = \frac{Le}{Pe} \left(\frac{d^2 \hat{T}}{d\hat{r}^2} + \frac{2}{\hat{r}} \frac{d\hat{T}}{d\hat{r}} \right) + \frac{1}{St} \left(\frac{d\hat{j}}{d\hat{r}} + \frac{2}{\hat{r}} \hat{j} \right), \quad (16)$$

$$\frac{d\hat{T}}{d\hat{r}} = -Li_p \hat{g} \hat{\rho} \hat{T} - \frac{Li_\xi St}{R_\rho} \hat{T}^2 \frac{d\hat{\xi}}{d\hat{r}}. \quad (17)$$

188 where the dimensionless numbers are defined as

$$R_\rho = \frac{\rho^{sl}}{\rho_-^s}, \quad R_v = \frac{\Delta V_{Fe}^{s,l}}{\Delta V_{Fe,O}^{s,l}}, \quad Li_p \equiv \frac{\Delta V_{Fe}^{s,l} g^{sl} \rho^{sl} r^{sl}}{L}, \quad Li_\xi \equiv \frac{1000 R \xi^{sl}}{a_O c_p},$$

$$Pe \equiv \frac{v_f r^{sl}}{D_O}, \quad St \equiv \frac{q^{sl}}{\rho_-^s v_f L}, \quad Le \equiv \frac{k}{\rho^{sl} c_p D_O}. \quad (18)$$

189 R_ρ is the ratio between the reference density and the density on the solid side of
 190 the ICB, and R_v is the ratio between the change in specific volumes upon phase
 191 change of pure iron and the iron alloy. The dimensionless numbers Li_p and
 192 Li_ξ arise from the pressure and compositional parts of the liquidus constraint
 193 (17), respectively. Pe is the Péclet number that measures the ratio between
 194 advection and chemical diffusion. St is the Stefan number and gives the ratio
 195 between sensible and latent heat. Le is the Lewis number that describes the
 196 ratio between thermal and chemical diffusivity.

197 Inserting the scalings (14) into (8)–(13) yields the dimensionless boundary

$$\hat{T}(1) = \frac{T^{sl} c_p R_\rho}{StL}, \quad (19)$$

$$\left. \frac{d\hat{T}}{d\hat{r}} \right|_{\hat{r}=\frac{r^i}{r^{sl}}} = -\frac{Pe}{StLe}, \quad (20)$$

$$\left. \frac{d\hat{T}}{d\hat{r}} \right|_{\hat{r}=1} = -\frac{Pe}{Le}, \quad (21)$$

$$\hat{\xi}(1) = 1, \quad (22)$$

$$\hat{j}\left(\frac{r^i}{r^{sl}}\right) = -\hat{v}, \quad (23)$$

$$\hat{j}(1) = 0. \quad (24)$$

199 2.4. Model parameters and constraints

200 We solve the dimensionless system numerically using `solve_bvp`, which is
 201 a boundary value problem solver included in `scipy` – an open source Python
 202 library [28]. We rewrite the problem as a system of first-order ODEs, and vary
 203 the model parameters Pe , St , Le , Li_p , Li_ξ , R_ρ , R_v and T^{sl} (see Table 1). The
 204 numerical code written to solve the slurry equations is freely available online
 205 [29]¹. Unless otherwise specified, all other physical properties of the F-layer
 206 are assumed constant, as specified in Table A.2.

207 Pe varies because of the range of seismic estimates of the F-layer thickness,
 208 d , and the unknown freezing speed, v_f . We obtain a proxy for v_f through the
 209 ICB heat flow, Q^s , which we presume cannot be much greater than the adiabatic
 210 value estimated as $Q^a = 1.6$ TW [14], though we allow a wider margin of Q^s up
 211 to 3.2 TW to account for uncertainties also inherent in the estimate of Q^a in the
 212 literature. St varies due to Q^s and Q^{sl} . While there is no geophysical constraint
 213 on Q^{sl} , we test Q^{sl} over a wide range up to 12 TW which is verified *a posteriori*

¹<https://github.com/jnywong/nondim-slurry>

214 to give $5 \leq Q^c \leq 17$ TW [7, 30] (see Appendix C for the calculation of Q^c). Le
215 depends on the thermal conductivity and we explore two values that represent
216 the higher and the lower estimates given in the literature [13, 21, 31]. Li_p and
217 R_ρ change according to the layer thickness and also the reference density, ρ^{sl} ,
218 though the density on the solid side of the ICB remains the same and is taken
219 from PREM, $\rho_-^s = 12,764$ kgm $^{-3}$. Li_ξ depends on ξ^{sl} , wherein the precise
220 amount of oxygen present in the bulk of the Earth’s core is difficult to constrain
221 with reported values varying between 0.1 and 11.0 mol.% for core chemistry
222 models that include other light elements in addition to oxygen [32]. Varying
223 ξ^{sl} between 2.0 and 12.0 mol.% changes R_v , which depends on both the layer
224 thickness and the CSB oxygen concentration and in turn affects the change in
225 specific volume between solid iron and the liquid iron alloy.

| Input parameter | Symbol | Units | F-layer |
|--|------------|-----------------------|------------------------------|
| Layer thickness | d | km | 150, 200, 250, 300, 350, 400 |
| Thermal conductivity | k | W m $^{-1}$ K $^{-1}$ | 30, 100 |
| ICB heat flux | Q^s | TW | 0 – 3.20 |
| CSB heat flux | Q^{sl} | TW | 0 – 12 |
| Sedimentation prefactor | k_ϕ | kgm $^{-3}$ s | $10^{-5} - 10^{-1}$ |
| CSB liquidus temperature | T^{sl} | K | 4,500 – 6,000 |
| CSB oxygen concentration | ξ^{sl} | mol.% | 2 – 12 |
| Péclet number | Pe | | 0 – 2500 |
| Stefan number | St | | 0 – 3 |
| Lewis number | Le | | 354 – 1196 |
| Liquidus number (pressure) | Li_p | | 0.163 – 0.220 |
| Liquidus number (compositional) | Li_ξ | | 0.004 – 0.028 |
| Ratio between solid and reference density | R_ρ | | 0.940 – 0.952 |
| Ratio between change in specific volumes upon phase change of pure iron and iron alloy | R_v | | 0.203 – 0.235 |

Table 1: Relevant dimensional and dimensionless parameter range for the F-layer, taking other physical parameters as constant given in Table A.2.

226 We constrain T^{sl} in boundary condition (19) from the melting curves of iron,
227 which is usually reported in the range of 5,500 K [33] to 6,350 K [34]. Light

228 elements present in the iron alloy depress the liquidus temperature of pure iron,
 229 and a typical value of $\Delta T_\xi = 700$ K is used, though this can also vary between
 230 500 and 1,000 K [32]. We therefore opt to vary T^{sl} between 4,500 and 6,000 K.

231 We constrain the results of the parameter study in three ways:

- 232 1. by the seismically determined density jump at the ICB [9]. The jump
 233 obtained from normal modes, $\Delta\rho_{\text{mod}}$, has a long wavelength on the order
 234 of hundreds of kilometres and represents the difference between the av-
 235 erage densities of the top of the inner core and the bottom of the outer
 236 core. The jump obtained from body waves, $\Delta\rho_{\text{bod}}$, has a short wavelength
 237 on the order of several kilometres, and therefore represents the difference
 238 in densities either side of the ICB. The difference between the normal
 239 mode and body wave estimates therefore points to a density anomaly
 240 caused by the F-layer. Normal mode studies suggest $600 \text{ kg m}^{-3} \leq$
 241 $\Delta\rho_{\text{mod}} \leq 820 \pm 180 \text{ kg m}^{-3}$ [2, 35], whereas body wave studies suggest
 242 $520 \pm 240 \text{ kg m}^{-3} \leq \Delta\rho_{\text{bod}} \leq 1,100 \text{ kg m}^{-3}$ [36, 37]. Hence solutions
 243 obtained from the slurry model should satisfy a maximum density jump
 244 across the layer of $\max(\Delta\rho_{\text{mod}} - \Delta\rho_{\text{bod}}) = 1,000 - 280 = 720 \text{ kg m}^{-3}$,
 245 and a minimum bound $\min(\Delta\rho_{\text{mod}} - \Delta\rho_{\text{bod}}) < 0$ is not specified since the
 246 seismic observations from different studies vary in their approaches, so we
 247 consider zero as the lower bound.
- 248 2. solutions should be consistent with estimates of the present-day CMB heat
 249 flux, which should be between 5 and 17 TW [7, 30]
- 250 3. we assess the stability of the layer and determine whether the solution is
 251 stable, partially stable or unstable, and reject solutions that are unstable.

252 To apply the constraints on density we calculate the density jump across the
 253 slurry layer, $\rho_+^s - \rho^{sl}$, where ρ_+^s is the density on the slurry side of the ICB. The

254 total density is

$$\rho = \rho_H + \rho', \quad (25)$$

255 where

$$\rho_H = \left(\frac{g}{K}(r - r^{sl}) + \frac{1}{\rho^{sl}} \right)^{-1}, \quad (26)$$

256 is the hydrostatic part, in which K denotes the bulk modulus, and

$$\rho' = \rho^{sl} \left[-\alpha T' - \alpha_\xi \xi^{l'} + (\alpha_\phi + \alpha_\xi \xi^l) \phi' \right]. \quad (27)$$

257 is the density perturbation, where T' , $\xi^{l'}$ and ϕ' are perturbations in the de-
258 composition

$$T = T^{sl} + T',$$

$$\xi^l = \xi^{sl} + \xi^{l'},$$

$$\phi = \phi^{sl} + \phi',$$

259 with $\phi^{sl} = 0$ at the CSB. In the equation of state (27), the first two terms are
260 well known from double diffusive/thermochemical convection theory, whereas
261 the last term is unique to the slurry. The expansion coefficient of the solid is
262 defined as

$$\alpha_\phi = \rho^{sl} \Delta V_{Fe,O}^{s,l},$$

263 (see derivation in Appendix D). To determine ϕ' , the dimensional solid flux
264 yielded from the solution of the slurry equations is related to the solid fraction
265 by

$$\mathbf{j} = b(\phi) \Delta V_{Fe,O}^{s,l} \nabla p. \quad (28)$$

266 We employ a Stokes' flow model of mobility [38] where we assume that the
 267 solid iron particles created in the slurry layer drift towards the ICB under the
 268 influence of gravity. Consequently the sedimentation coefficient is given by

$$b(\phi) = k_\phi \phi^{5/3} = \left(\frac{\rho_-^s (\rho^{sl})^2}{162\pi^2 \nu^3 N^2} \right)^{1/3} \phi^{5/3}, \quad (29)$$

269 where N is the number of particles in a unit volume. We write k_ϕ to group
 270 the prefactors that multiply the solid fraction. This k_ϕ sedimentation prefactor
 271 introduces a degree of freedom since N and the value of the kinematic viscosity,
 272 ν , in the slurry is unknown. We further consider this issue in Section 3.2, where
 273 we conduct a sensitivity analysis on k_ϕ .

274 We evaluate the gradient of the density perturbations to assess the stability
 275 of the layer. Solving the slurry equations yields T , ξ^l and ϕ and subtracting
 276 the reference values from these quantities gives the perturbations T' , ξ^l and ϕ' ,
 277 which allows us to evaluate the density perturbation (27). If the layer is stable
 278 then the change in density relative to the hydrostatic reference should decrease
 279 as the radius increases, i.e. $d\rho'/dr < 0$, and vice versa if the layer is unstable,
 280 i.e. $d\rho'/dr > 0$. We relax the condition for stability slightly by stipulating that
 281 the layer is partially stable if $d\rho'/dr < 0$ for at least 100 km of the layer since
 282 the seismic resolution from normal modes is on the order of this value.

283 3. Results and discussion

284 3.1. Example solution

285 Figure 2 shows example solutions for a wide range of layer thicknesses be-
 286 tween 150 and 400 km, where $Q^s = 2.5$ TW ($v_f = 0.44$ mmyr⁻¹), $Q^{sl} = 5$ TW,
 287 $k = 100$ Wm⁻¹K⁻¹ and $T^{sl} = 5,547$ K taken from [25, 27], for an 82%Fe-8%O-
 288 10%Si mixture. For all layer thicknesses the temperature gradient is strictly

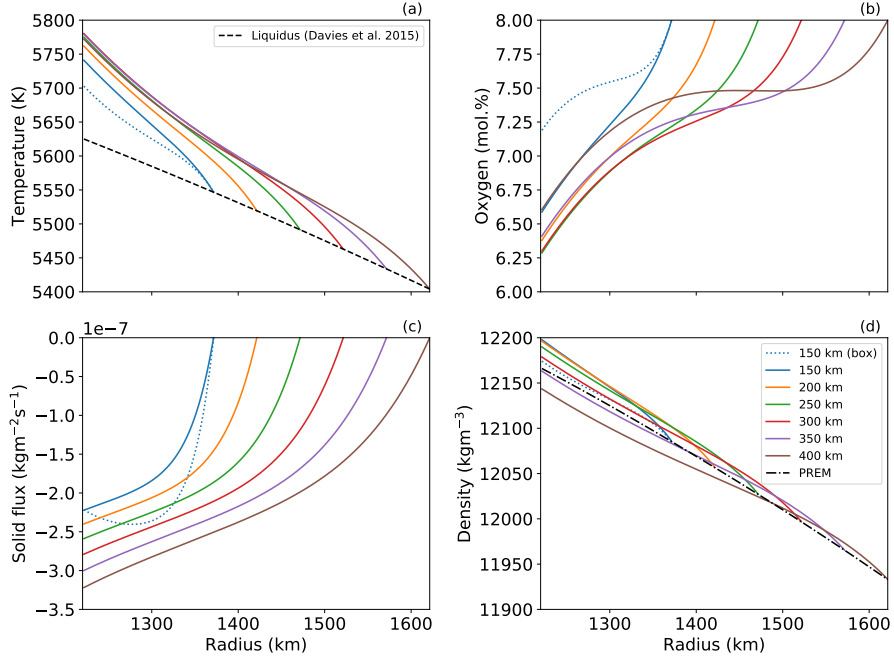


Figure 2: Profiles of (a) temperature, (b) oxygen concentration, (c) solid flux and (d) density across the slurry with layer thicknesses between 150 and 400 km. The dashed line in (a) is the uniform composition liquidus determined from *ab initio* calculations [25, 27], and the dash-dotted line in (d) is the PREM density [2]. The blue dotted line is the equivalent box model case from W18 for $d = 150$ km (see text). Control parameters are $Q^s = 2.5$ TW, $Q^{sl} = 5.0$ TW, $k = 100$ Wm⁻¹K⁻¹ and $T^{sl} = 5,547$ K (colour online).

289 negative so the slurry is thermally destabilising, whereas the compositional gra-
 290 dient may either be stable or unstable. Solid flux is always negative in the
 291 direction towards the ICB, achieving its largest magnitude at the ICB itself
 292 and then vanishing to zero at the top of the layer as imposed by the boundary
 293 condition (24). Temperature, oxygen and solid flux all contribute to the overall
 294 density across the layer and the layer is stably-stratified when $150 \leq d \leq 300$ km,
 295 however for $d \geq 350$ km the layer is unstable.

296 We observe in Figure 2(c) that the solid flux eventually increases exponen-
 297 tially with radius under the influence of turbulent mixing from the bulk of the
 298 liquid outer core. As the solid flux diminishes its gradient sharply increases,

299 equivalent to precipitating more iron particles. The latent heat release associ-
 300 ated with the phase change in the sublayer prompts the slurry to depress the
 301 temperature in Figure 2(a) to stay on the liquidus and the oxygen concentration
 302 gradient increases in response to this as seen in Figure 2(b).

303 For completeness, we compare the solution in spherical geometry for $d =$
 304 150 km with the equivalent boundary conditions from the Cartesian geometry of
 305 W18, except for the box model we have shifted the CSB temperature to coincide
 306 with the liquidus value from [25, 27]. The main difference is that the effect of
 307 spherical geometry suppresses the effect of the mixing sublayer, since Figure
 308 2(c) shows that the solid flux gradient in the upper part of the layer is shallower
 309 than the box model case. Melting at the base of the layer in the box model is
 310 highlighted by the negative gradient in the solid flux, which is not present in the
 311 spherical model, and contributes positively to the density variations at the base
 312 of the layer in the box model. Despite this, turbulent mixing in the sublayer
 313 dominates to depress the temperature and oxygen variations, producing a much
 314 smaller density difference overall in the box model.

315 The control parameters Pe and Li_p depend linearly on d and parameters
 316 R_ρ , R_v and Le depend indirectly on d through ρ^{sl} . For a sense of scale in the
 317 variation of parameters from $d = 150$ km to 400 km for the reference solution
 318 given in Figure 2, Pe increases by 18%, Li_p increases by 35%, R_v increases
 319 by 14% and the changes in R_ρ and Le are less than 1.5%. The combined
 320 effect of these changes strengthens the decay in temperature as a function of
 321 radius over the bulk of the layer (excluding the mixing sublayer), as seen in
 322 Figure 2(a), but decreases F and the strength of the turbulent mixing layer
 323 through the barodiffusion term in (15), as seen in Figure 2(c), which combine
 324 to reduce the magnitude of the density variations in the layer overall. Figure
 325 3 shows more clearly that contributions to $d\rho'/dr$ from the oxygen gradient for

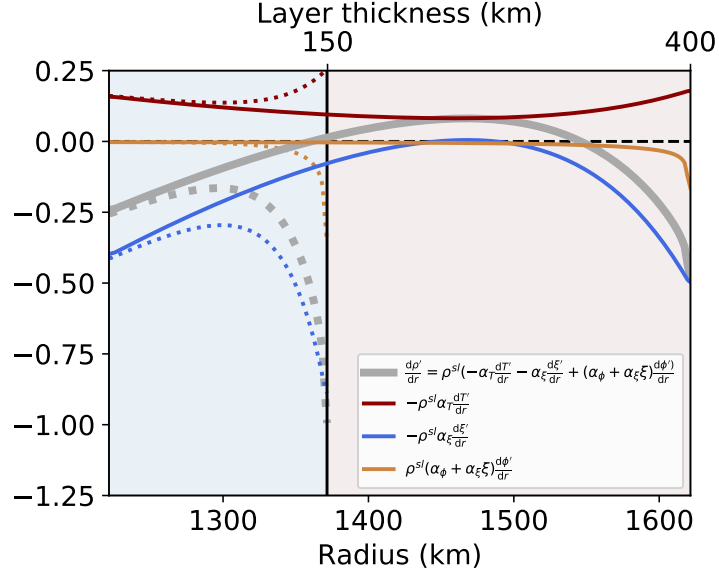


Figure 3: Gradients of the density variation (grey), $d\rho'/dr$, separated into contributions from the temperature (red), $-\rho^{sl}\alpha_T dT'/dr$, oxygen (blue), $-\rho^{sl}\alpha_\xi d\xi'/dr$, and solid fraction (orange), $\rho^{sl}(\alpha_\phi + \alpha_\xi \xi)d\phi'/dr$, across the slurry for layer thicknesses of 150 (dotted) and 400 km (solid). If $d\rho'/dr < 0$ the slurry is stable, whereas if $d\rho'/dr > 0$ the slurry is unstable. Control parameters are $Q^s = 2.5$ TW, $Q^{sl} = 5.0$ TW and $k = 100$ Wm $^{-1}$ K $^{-1}$ (colour online).

326 $d = 400$ km can become positive in the mid-depths, since the pressure part of the
327 liquidus relation (17) outweighs the temperature part, before becoming negative
328 again under the stabilising influence of the mixing sublayer. Oxygen variations
329 predominantly control the gradient of the density variations. When $d = 400$ km
330 the sign of $d\rho'/dr$ changes from negative (stable), to positive (unstable), and
331 back to negative again, producing an “S”-shaped density profile seen in Figure
332 2(d). On the other hand, Figure 3 shows that for $d = 150$ km the layer is stable
333 since $d\rho'/dr < 0$ throughout the layer. Overall variations in the solid fraction,
334 ϕ' , are negligible over the majority of the layer, perhaps apart from a very thin
335 region at the top (see Appendix B for further discussion on $d\phi$).

336 *3.2. Sensitivity analysis*

337 We evaluate the sensitivity of the slurry system to the sedimentation pref-
338 actor, k_ϕ , CSB temperature, T^{sl} , and CSB oxygen concentration, ξ^{sl} . We vary
339 the value of k_ϕ by a large range between 10^{-5} and 10^{-1} kgm^{-3}s and recompute
340 the example given in Figure 2(a) where the layer thickness is fixed at 150 km.
341 Figure 4(a) shows that density stratification is increased with smaller values of
342 k_ϕ and the solutions converge as k_ϕ exceeds 10^{-3} kgm^{-3}s . Figure 4(b) shows
343 the corresponding solid fraction, ϕ , profiles within the layer. It can be seen
344 that for the smallest value of k_ϕ , the solid fraction is close to the rheological
345 transition at $\phi_m = 0.6$ [39], which violates the assumption that $\phi \ll 1$ in the
346 slurry. We select a value of $k_\phi = 10^{-2}$ kgm^{-3}s that is high enough so that the
347 density becomes independent of k_ϕ and consistent with $\phi \ll 1$ in the slurry.

348 For the CSB temperature, we recompute the example case with $d = 150$ km
349 and vary T^{sl} between 4,500 and 6,000 K with intervals of 100 K and for the
350 CSB oxygen concentration we vary its value between 2.0 and 12.0 mol.% with
351 intervals of 0.5 mol.%. Figure 5(a) and (b) presents the density profiles across
352 the layer with varying T^{sl} and ξ^{sl} , respectively. We find that no solutions were
353 obtained for values below $\xi^{sl} = 2.0$ mol.%. Figure 5(b) shows that despite the
354 variation in ξ^{sl} , there appears to be a limited effect on the resulting density pro-
355 files, whereas Figure 5(a) shows that changing T^{sl} introduces a greater spread
356 in the solutions obtained. In terms of the dimensionless parameters, varying
357 $2.0 \text{ mol.\%} < \xi^{sl} < 12.0 \text{ mol.\%}$ through $0.004 < Li_\xi < 0.028$ does not signifi-
358 cantly affect the system, where Li_ξ enters into the pressure part of the liquidus
359 relation and the barodiffusion term of equation (15). Changing T^{sl} in boundary
360 condition (19) shifts the anchor point of the temperature solution and will not
361 affect the curvature of the temperature profile since the heat fluxes into and out
362 of the slurry remain fixed, so the temperature perturbations are the same for

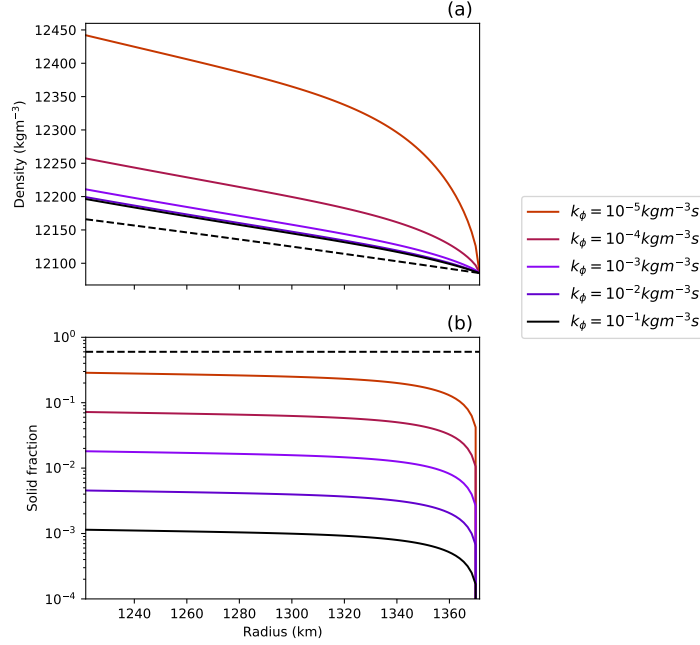


Figure 4: (a) Density and (b) solid fraction profiles across the layer for different values of k_ϕ . The dashed line in (a) is PREM and the dashed in (b) is $\phi_m = 0.6$ that defines the rheological transition [39]. All other input parameters are the same as the case in Figure 2 with the layer thickness fixed at 150 km (colour online).

363 all T^{sl} . However, T^{sl} does affect the oxygen concentration through the liquidus
 364 relation, where a higher T^{sl} will decrease the oxygen concentration gradient and
 365 create smaller perturbations in the oxygen concentration, therefore generating
 366 smaller density perturbations to produce a lower slurry density overall. A lower
 367 T^{sl} has the opposite effect to produce a higher slurry density. The spread in the
 368 ICB density with different T^{sl} is roughly 60 kgm^{-3} , and there is up to a 40%
 369 change in the density jump across the whole layer with respect to the example
 370 case. This sensitivity may have an impact on the overall stability of the layer,
 371 however for the regime diagram we shall continue to use the default value from
 372 the literature of $T^{sl} = 5,547 \text{ K}$ for a layer 150 km thick.

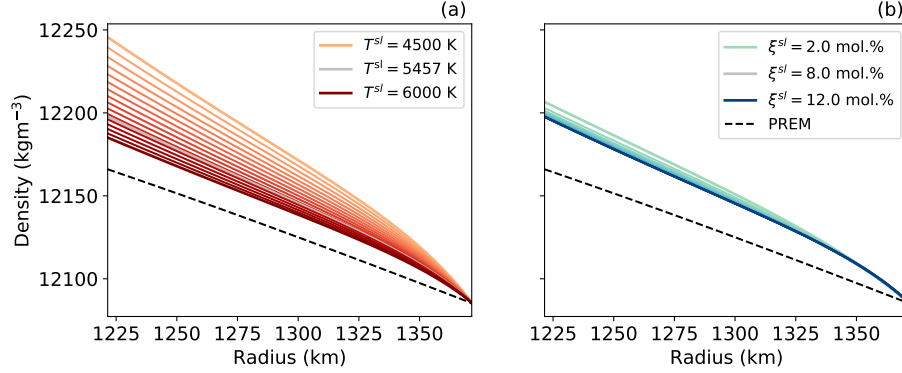


Figure 5: Density profiles across the layer for (a) $4,500 < T^{sl} < 6,000$ K and (b) $2.0 < \xi^{sl} < 12.0$ mol.%. Default values of $T^{sl} = 5,547$ K from [25, 27] in (a) and $\xi^{sl} = 8.0$ mol.% in (b) are given by the grey lines. All other input parameters are the same as the example case, and the layer thickness is fixed at 150 km (colour online).

373 3.3. Regime diagram

374 We present a regime diagram of the Pe, St -space by varying Q^s and Q^{sl} .

375 There are two cases: high thermal conductivity, $k = 100 \text{ Wm}^{-1}\text{K}^{-1}$, corre-
 376 sponding to $Le = 1181$ and low thermal conductivity, $k = 30 \text{ Wm}^{-1}\text{K}^{-1}$,
 377 corresponding to $Le = 354$. By fixing $d = 150$ km and $\xi^{sl} = 8$ mol.%, then
 378 $Li_p = 0.16$, $Li_\xi = 0.018$, $R_\rho = 0.952$ and $R_v = 0.235$.

379 Figure 6(a) and (c) presents the regime diagram for the high Lewis number
 380 case, and Figure 6(b) and (d) is the regime diagram for the low Lewis number
 381 case. Regions of the phase space are divided into stable ($d\rho'/dr < 0$), partially
 382 stable ($d\rho'/dr < 0$ for at least 100 km) and unstable ($d\rho'/dr > 0$) slurries, and
 383 also areas with no slurry where no solution is found.

384 No slurry can exist when the latent heat release at the ICB interface exceeds
 385 the CSB heat flux, so that

$$\text{if } Q^{sl} < Q^s \quad \text{then} \quad St = \frac{q^{sl}}{q^s} < \left(\frac{r^i}{r^{sl}} \right)^2 \equiv St^*$$

386 which corresponds to a critical Stefan number of $0.6 \leq St^* \leq 0.8$ for 150 km \leq

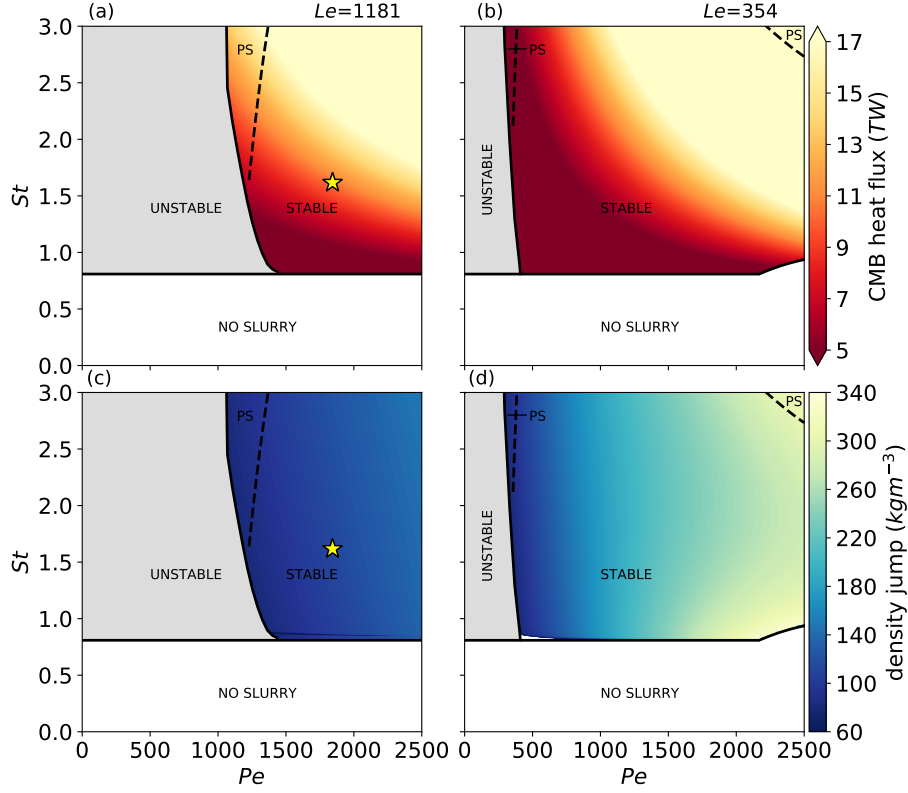


Figure 6: (Left column) Regime diagrams for the high Lewis number case, (right column) and the low Lewis number case with $d = 150$ km. (Top row) Contours of the CMB heat flux constrained by $5 < Q^c < 17$ TW and (bottom row) contours of the density jump, $\rho_+^s - \rho^{sl}$. The phase space is divided into stable (contour fill), partially stable, denoted PS (contour fill, dashed line), unstable (grey) and no slurry (white) regions. The yellow star represents the example case from Figure 2 (colour online).

387 $d \leq 400$ km. When the layer thickness is 150 km, above $St^* = 0.8$ we find a
 388 region of unstable solutions at lower Pe and stable solutions at higher Pe , and
 389 this transition generally occurs when

$$Pe_T \equiv \frac{Pe}{Le} = \frac{v_f r^{sl}}{\kappa} \simeq 1, \quad (30)$$

390 where Pe_T is the thermal Péclet number and $\kappa = k/\rho^{sl}c_p$ is the thermal dif-
 391 fusivity. Pe_T controls the boundary condition on the temperature gradient in

392 (20) and (21). An unstable slurry develops when $Pe < Le$ because more heat
 393 is conducted through the slurry which is unavailable for equilibration through
 394 the liquidus constraint, hence creating a smaller oxygen concentration difference
 395 that produces a smaller density contrast that is insufficient to stabilise the layer.
 396 A stable slurry develops when $Pe > Le$ as the rate of advection from the com-
 397 pacting layer overcomes the thermal diffusion rate. Increasing Pe_T stabilises the
 398 slurry layer since the temperature gradient steepens at the boundaries, therefore
 399 generating greater positive variations in the oxygen gradient that enhance the
 400 density anomaly. If $d = 150$ km then the transition at $Pe \simeq Le$ corresponds
 401 to $Q^s = 1.5$ TW for high Le and $Q^s = 0.5$ TW for low Le . Figure 6(c) and
 402 (d) show that the density jump across the layer in all cases is well below the
 403 maximum limit of 720 kgm^{-3} and also suggests that the density jump roughly
 404 scales with Pe , with higher values encountered at low Le .

405 A higher St steepens the CSB temperature gradient relative to the ICB, and
 406 condition (30) is met by strengthening the turbulent sublayer at the top of the
 407 slurry by increasing the mixing parameter F . Within the sublayer the rate of
 408 crystallisation is increased, therefore the density jump across the layer increases
 409 with St as seen in Figure 6(c) and (d). The critical Pe_T where the slurry
 410 transitions from unstable to stable slightly decreases as St increases and the
 411 layer is more likely to become partially stable. We find that the dimensionless
 412 ICB speed, and thereby the magnitude of the solid flux at the ICB, is roughly
 413 proportional to St . The ICB speed affects contributions to the secular cooling,
 414 gravitational power and latent heat release in the core and therefore influences
 415 the total CMB heat flow. This is reflected in Figure 6(a) and (b) on the total
 416 CMB heat flux, which scales linearly with $PeSt$.

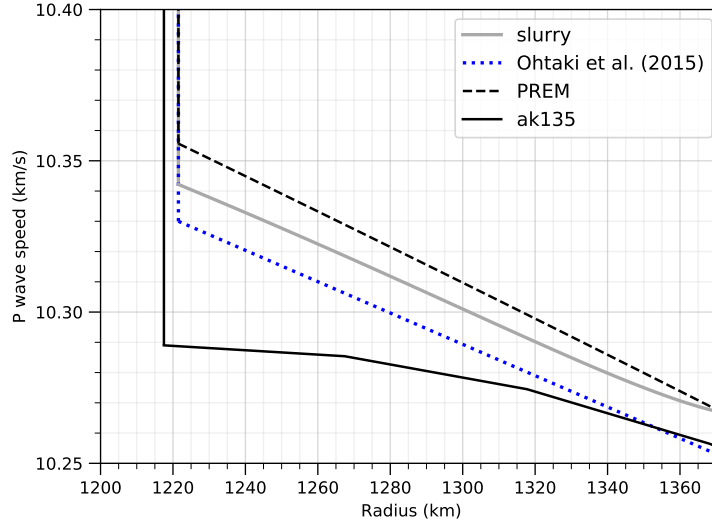


Figure 7: P wave speed in the F-layer derived from the high Le example solution with $d = 150$ km, $k = 100 \text{ Wm}^{-1}\text{K}^{-1}$, $Q^s = 2.5 \text{ TW}$ and $Q^{sl} = 5.0 \text{ TW}$ (grey, solid). Seismic models are PREM (black, dashed), ak135 (black, solid) and the FVW model of Ohtaki *et al.* [4] (blue, dotted) (colour online).

418 Motivated by the seismic observations, we have demonstrated that a slurry is
 419 able to produce stable layers with varying degrees of stratification depending on
 420 the parameters selected. If we invert the process, then what constraints can the
 421 model provide on observations? From our slurry model we can determine the
 422 density at every point across the layer and hence the P wave speed, $v_p^2 = K/\rho$.
 423 The bulk modulus, K , depends on the core chemistry and therefore an appro-
 424 priate equation of state should be applied [19, 40]. For the sake of simplicity we
 425 approximate the bulk modulus by PREM in our calculations.

426 Figure 7 illustrates the v_p profile of the example solution from Section 3.1
 427 compared with the seismic models of PREM [2], ak135 [41] and the FVW model
 428 of Ohtaki *et al.* [4]. The P wave speed from the slurry model is reduced relative
 429 to PREM by up to 0.13% and there is a difference of 0.1% compared with
 430 Ohtaki *et al.* [4], which reported that $v_p(r^i) = 10.3 \text{ km s}^{-1}$ and $dv_p/dr =$

431 $-5.2 \times 10^{-7} \text{ s}^{-1}$. For this example slurry solution we obtain a density jump
432 across the layer of $\rho_+^s - \rho^{sl} = 112 \text{ kg m}^{-3}$ and calculate that $Q^c = 10.4 \text{ TW}$, which
433 is within the acceptable range of CMB heat flows. On the slurry side of the ICB
434 we have $\rho_+^s = 12,198 \text{ kg m}^{-3}$, therefore we predict that the density jump from
435 body waves for this particular slurry is $\Delta\rho_{\text{bod}} = \rho_-^s - \rho_+^s = 502 \text{ kg m}^{-3}$. The
436 density jump from normal modes is $\Delta\rho_{\text{mod}} = \Delta\rho_{\text{bod}} + \rho_+^s - \rho^{sl} = 628 \text{ kg m}^{-3}$,
437 and this is fixed in all solutions of the slurry by choosing ρ_-^s and ρ^{sl} from PREM.

438 Note that the example solution given above is one of many compatible
439 solutions given by the regime diagram. By considering the entire range of
440 parameters permitted by the regime diagram that fit with the geophysical
441 constraints, the high Le case gives $81 \leq \rho_+^s - \rho^{sl} \leq 140 \text{ kg m}^{-3}$ and the
442 low Le case gives $101 \leq \rho_+^s - \rho^{sl} \leq 331 \text{ kg m}^{-3}$. This leads to bounds of
443 $475 \leq \Delta\rho_{\text{bod}} \leq 534 \text{ kg m}^{-3}$ and $283 \leq \Delta\rho_{\text{bod}} \leq 513 \text{ kg m}^{-3}$ for high and low Le
444 respectively. The observations available give $520 \pm 240 \leq \Delta\rho_{\text{bod}} \leq 1,100 \text{ kg m}^{-3}$,
445 therefore our model suggests that a stably-stratified F-layer is opposed to the
446 higher values of $\Delta\rho_{\text{bod}}$ recommended by the observations and that the slurry
447 model gives an upper bound of $\Delta\rho_{\text{bod}} \leq 534 \text{ kg m}^{-3}$ for both Le cases.

448 We can approximate the inner core age using the model output of the ICB
449 speed, v , by assuming that inner core growth is proportional to the square-root
450 of time [42],

$$r^i(\tau) = r_0^i \left(1 + \frac{\tau}{\tau^i}\right)^{\frac{1}{2}}, \quad (31)$$

451 where τ is time normalised by the age of the inner core, τ^i , and r_0^i is the present-
452 day IC radius. By differentiating (31) and considering the present-day where
453 $\tau = 0$, we have

$$\tau^i = \frac{r_0^i}{2v}, \quad (32)$$

454 where we recall that $v \equiv v_f + v_s = dr^i/d\tau$ is the inner core growth rate.
 455 Estimating τ^i is of significant geophysical interest and its value is subject to
 456 debate since τ^i is directly related to the evolution of the core global heat balance,
 457 which is significantly affected by the thermal conductivity [21]. For the same
 458 range of solutions considered above to estimate $\Delta\rho_{\text{bod}}$, our results from the
 459 regime diagram for high Le give $0.52 \leq v \leq 0.98 \text{ mm yr}^{-1}$, which is relatively
 460 fast compared to the low Le solutions where $0.24 \leq v \leq 0.31 \text{ mm yr}^{-1}$. This
 461 yields an inner core age of $0.6 \leq \tau^i \leq 1.2 \text{ Ga}$ for high Le , which is in line
 462 with other estimates from the literature [7], and $2.0 \leq \tau^i \leq 2.6 \text{ Ga}$ for low Le ,
 463 which is mostly beyond oldest estimates of 2.0 Ga from the literature using low
 464 thermal conductivity [27]. Our results therefore suggest a slurry model with
 465 high core conductivity predicts geophysical properties of the F-layer and core
 466 that are consistent with independent seismic and geodynamic calculations.

467 4. Conclusions

468 In this study, we have investigated the conditions that produce a stably-
 469 stratified slurry layer at the base of the Earth's outer core. We non-dimensionalise
 470 the governing equations given by W18 and elucidate the key dimensionless pa-
 471 rameters that control the system behaviour. By varying the Péclet and Stefan
 472 numbers, we map a regime diagram of the slurry demarcating the conditions
 473 that favour stable, partially stable and unstable density configurations, as well
 474 as no slurry. Solutions are obtained for high and low Le numbers, which reflect
 475 high or low thermal conductivity values of the core. We constrain the results
 476 by evaluating the density jump across the layer and the total CMB heat flux.

477 Our main result is that stably-stratified solutions can be produced by a slurry
 478 for a wide range of parameters that span plausible values for Earth's core. We
 479 have identified regions of the parameter space containing many solutions that

480 are compatible with observations of the F-layer, and we have also established
481 conditions that are not suitable. We find that

- 482 • $Pe_T = \frac{Pe}{Le} \simeq 1$ divides the space between unstable and stable slurry layers,
- 483 • higher Péclet number slurries generally facilitate stable density stratifica-
484 tion because this controls the steepness of the temperature gradient at the
485 boundaries, which in turn increases the magnitude of density variations in
486 the slurry,
- 487 • the Stefan number has a stabilising role through crystallising more parti-
488 cles in the turbulent mixing sublayer,
- 489 • no slurry can exist with $St < St^* = (r^i/r^{sl})^2$ since the heat flow at the
490 bottom of the layer is greater than at the top of the layer
- 491 • the slurry model suggests that $\Delta\rho_{\text{bod}} \leq 534 \text{ kg m}^{-3}$ for high and low Le
- 492 • estimates of the inner core age suggests a slurry with high core conduc-
493 tivity is compatible with independent estimates from the literature

494 Density perturbations of compositional origin dominate contributions to the
495 overall stability of the layer, and can be destabilised through increasing the layer
496 thickness. We have also investigated the sensitivity to the CSB temperature and
497 oxygen concentration and deduced a limit for the prefactor $k_\phi = 10^{-2} \text{ kgm}^{-3}\text{s}$
498 that defines the sedimentation coefficient, $b(\phi)$, which relates the solid flux, \mathbf{j} , to
499 the solid fraction, ϕ , through Stokes' flow. We find that the model is insensitive
500 to the concentration of oxygen at the CSB, however, the effect of the liquidus
501 temperature is significant to the overall stability of the layer.

502 From mineral physics or seismology of model uncertainties, improved esti-
503 mates such as the layer thickness, CSB temperature and the CSB oxygen con-
504 centration, will benefit the slurry model greatly. Further progress determining

505 the liquidus curve for an iron mixture, using experiments or first-principle cal-
506 culations, could improve the temperature condition at the CSB, and improved
507 estimates of the density jump across the layer from normal and body wave
508 studies would help constrain the space of geophysically consistent solutions.

509 We examined the P wave speed in the slurry layer to show that the model
510 can produce a profile that compares well with other seismic models. This could
511 be further verified comprehensively so that the model may provide a useful tool
512 for corroborating observations, such as constraining the seismic density jump
513 at the ICB derived from body waves, $\Delta\rho_{\text{bod}}$. There is also the potential for
514 the slurry to provide improved and independent estimates of the inner core age
515 stipulated by having a stable F-layer that agrees with the seismic and heat flow
516 requirements.

517 We implemented a simple compacting layer on the solid side of the IC where
518 solid particles produced by the slurry accumulate and instantly compact. Re-
519 alistically the physics of this process is extremely complicated. Studies suggest
520 that a mush solidification regime can occur [6] where liquid channels permeate a
521 matrix of solid with a high solid fraction. A more advanced model may seek to
522 incorporate this process. The timescale of interest in our slurry is comparable
523 to the slow growth of the inner core, where we have applied the fast melting
524 limit. On short timescales at the microscopic level, the effect of supercooling
525 on the nucleation of solid iron at core conditions may come into play and this
526 topic is an active area of interest [43, 44, 45].

527 Future work could focus on assessing the dominant balances between terms
528 in the slurry equations that are responsible for stable density stratification so
529 that the physics controlling the transitions between different regimes can be
530 elucidated. For example, the importance of the mixing sublayer and its influence
531 on the production of solid phase needs to be quantitatively evaluated. A more

532 sophisticated model coupling the slurry to outer core convection, perhaps similar
533 to a recent study conducted by Bouffard *et al.* [46] for the stably-stratified layer
534 at the top of the core, may fully capture the physics of this process and shed
535 light on the effect of entrainment.

536 Our study also opted to keep the layer thickness constant over time in order
537 to ascertain solutions that are concomitant with the present-day seismic obser-
538 vations. Relaxing the layer thickness requires an extra constraint on the model
539 to be developed in its place [47]. Constructing a fully time-dependent frame-
540 work could provide insight into the factors controlling the growth and decline
541 of a slurry layer, which may shed light on how the F-layer came into existence
542 over the core’s history.

543 **5. Acknowledgements**

544 The numerical code used to solve the slurry equations in this paper is freely
545 available at <https://github.com/jnywong/nondim-slurry> [29]. We thank
546 Marine Lasbleis and an anonymous reviewer for their constructive comments
547 that helped improve this paper. JW acknowledges support from the Fondation
548 Simone and Cino Del Duca of Institut de France and the Engineering and Phys-
549 ical Sciences Research Council (EPSRC) Centre for Doctoral Training in Fluid
550 Dynamics (EP/L01615X/1). CJD is supported by the Natural Environment
551 Research Council (NERC) Independent Research Fellowship (NE/L011328/1).
552 Figures were produced using Matplotlib [48].

553 **Appendix A. Table of values**

| Symbol | Definition | Value | Units | Source |
|------------|---|-------|--------------------------------|--------|
| p | Pressure | | $\text{kgm}^{-1}\text{s}^{-2}$ | |
| T | Temperature | | K | |
| ξ | Light element concentration | | Mass fraction | |
| ξ^l | Light element concentration in the liquid phase | | Mass fraction | |
| ϕ | Solid fraction | | Mass fraction | |
| j | Solid flux | | $\text{kgm}^{-2}\text{s}^{-1}$ | |
| ρ | Density | | kgm^{-3} | |
| F | Mixing parameter | | | |
| v | ICB speed | | ms^{-1} | |
| v_f | Freezing speed | | ms^{-1} | |
| v_s | Snow speed | | ms^{-1} | |
| μ | Chemical potential | | Jkg^{-1} | |
| ρ_H | Hydrostatic density | | kgm^{-3} | |
| ρ' | Density perturbation | | kgm^{-3} | |
| T' | Temperature perturbation | | K | |
| $\xi^{l'}$ | Light element perturbation in the liquid phase | | Mass fraction | |
| ϕ' | Solid fraction perturbation | | Mass fraction | |

| | | | | |
|-----------|--|--------------------|-----------------------------------|----------|
| $b(\phi)$ | Sedimentation coefficient | | kgm^{-3}s | |
| k_ϕ | Sedimentation coefficient prefactor | | kgm^{-3}s | |
| ν | Kinematic viscosity | | m^2s^{-1} | |
| N | No. of solid iron particles per unit volume | | | |
| Φ | Gibbs free energy | | | |
| Pe | Péclet number | | | |
| St | Stefan number | | | |
| Le | Lewis number | | | |
| Li_p | Liquidus number (pressure) | | | |
| Li_ξ | Liquidus number (composition) | | | |
| R_ρ | Ratio between liquid and solid iron | | | |
| R_v | Ratio between the change in specific volumes upon phase change from pure iron and iron alloy | | | |
| R | Ideal gas constant | 8.31 | $\text{Jkg}^{-1}\text{mol.}^{-1}$ | |
| a_O | Atomic weight of oxygen | 16 | Da | |
| r^i | ICB radius | 1221×10^3 | m | PREM [2] |

| | | | | |
|--------------|---|--|--------------------------------|------------|
| d | Layer thickness | (150, 200, 250, 300, 350, 400) $\times 10^3$ | m | [3], [5] |
| r^{sl} | CSB radius | 1371–1621 $\times 10^3$ | m | [3], [5] |
| ρ_-^s | Density of iron on the solid side of the ICB | 12.76×10^3 | kgm^{-3} | PREM [2] |
| ρ_+^s | Density of iron on the liquid side of the ICB | | kgm^{-3} | |
| ρ^{sl} | Density of liquid iron at $r = r^{sl}$ | | kg m^{-3} | PREM [2] |
| g | Gravity | | ms^{-2} | PREM [2] |
| K | Bulk modulus | | $\text{kgm}^{-1}\text{s}^{-2}$ | PREM [2] |
| ξ^{sl} | Oxygen concentration in the bulk of the liquid core | 2–12 | mol.% | [32] |
| T^{sl} | Liquidus temperature at the CSB | 4,500–6,000 | K | [27, 25] |
| c_p | Specific heat capacity | 715 | $\text{Jkg}^{-1}\text{K}^{-1}$ | [23] |
| α | Thermal expansion coefficient | 1×10^{-5} | K^{-1} | [23] |
| α_ξ | Compositional expansion coefficient of oxygen | 1.1 | | [24] |
| L | Latent heat of fusion | 0.75×10^6 | Jkg^{-1} | [23] |
| k | Thermal conductivity | 30, 100 | $\text{Wm}^{-1}\text{K}^{-1}$ | [21], [27] |

| | | | | |
|-------------------------|--|-----------------------|----------------------------|-----------------------|
| \bar{D} | Modified self-diffusion coefficient of oxygen | | m^2s^{-1} | |
| D_O | Self-diffusion coefficient of oxygen | 0.98×10^{-8} | m^2s^{-1} | [25] |
| V_{Fe}^s | Specific volume of solid iron | | m^3kg^{-1} | Ideal solution theory |
| $V_{Fe,O}^l$ | Specific volume of liquid iron and oxygen | | m^3kg^{-1} | Ideal solution theory |
| $\Delta V_{Fe,O}^{s,l}$ | Change in specific volume between liquid and solid phase | | m^3kg^{-1} | Ideal solution theory |
| $\Delta V_{Fe}^{s,l}$ | Change in specific volume between liquid iron and solid iron | | m^3kg^{-1} | Ideal solution theory |
| α_ϕ | Expansion coefficient of solid | | | Ideal solution theory |
| q^s | ICB heat flow per unit area | | Wm^{-2} | |
| q^{sl} | CSB heat flow per unit area | | Wm^{-2} | |
| Q^s | ICB heat flow | | TW | |
| Q^{sl} | CSB heat flow | | TW | |
| Q^c | CMB heat flow | 5–17 | TW | [30], [7] |
| Q_s | Secular cooling | | TW | |
| Q_g | Gravitational power | | TW | |
| Q_l | Latent heat power | | TW | |

Table A.2: Symbols and values (if applicable) used in the slurry model. Group 1: fundamental thermodynamic variables. Group 2: slurry notation. Group 3: Dimensionless numbers. Group 4: Physical constants. Group 5: Seismic properties. Group 6: Properties determined from *ab initio* calculations and high-pressure experiments. Group 7: Properties that assume ideal solution theory. Group 8: Heat flow estimates.

554 Appendix B. Variations in the solid fraction, $d\phi$

555 We suppose that the variations in the solid fraction, $d\phi$, are negligible. Here
 556 we assess the validity of this assumption *a posteriori*. The variation in solid
 557 fraction enters the energy equation (2) and the equation of state (27). In the
 558 first instance, including these variations adds an extra term to the latent heat
 559 release due to phase change. The dimensionless energy equation (16) becomes

$$-\hat{v} \frac{d\hat{T}}{d\hat{r}} = \frac{Le}{Pe} \left(\frac{d^2\hat{T}}{d\hat{r}^2} + \frac{2}{\hat{r}} \frac{d\hat{T}}{d\hat{r}} \right) + \frac{1}{St} \left(\frac{d\hat{j}}{d\hat{r}} + \frac{2}{\hat{r}} \hat{j} - R_\rho \frac{d\phi}{d\hat{r}} \right).$$

560 Using the control parameters from Figure 3, we compare the order of magnitude
 561 of each part of the last term in the expression above where the $d\phi/d\hat{r}$ term ap-
 562 pears. In Figure B.8 we can see that with $r^i/r^{sl} = 0.89$ and 0.75 (corresponding
 563 to $d = 150$ and 400 km, respectively), the extra term due to the variations in ϕ
 564 is almost three orders of magnitude smaller compared with the other two terms
 565 in the majority of the layer. We observe that $|\frac{2}{\hat{r}}\hat{j}| \sim |R_\rho \frac{d\phi}{d\hat{r}}|$ approaching the top
 566 of the layer, which is a consequence of \hat{j} tending to 0 as dictated by boundary
 567 condition $\hat{j}(1) = 0$ in equation (24). This occurs within a very thin region at
 568 the top of the layer and so $|R_\rho \frac{d\phi}{d\hat{r}}|$ makes a negligible difference to the overall
 569 energy balance in the slurry.

570 Turning to the equation of state we observe that the contributions from the
 571 variations in solid also arise by imposing boundary condition (24), which can

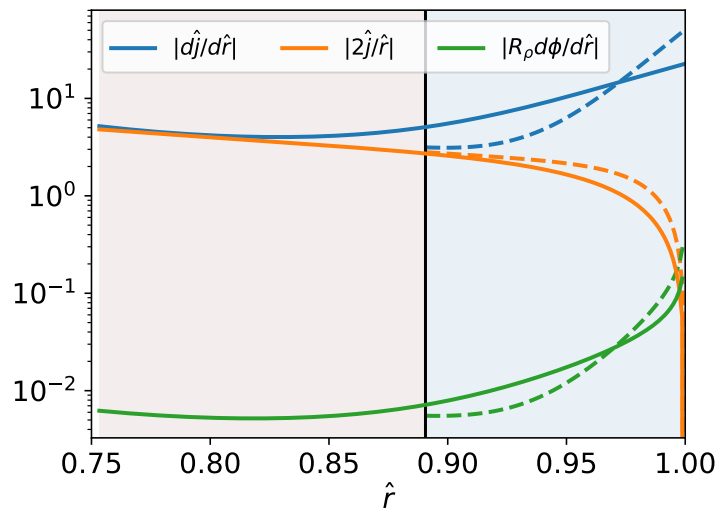


Figure B.8: Comparing magnitudes $|\frac{d\hat{j}}{d\hat{r}}|$, $|\frac{2}{\hat{r}}\hat{j}|$ and $|R_\rho \frac{d\phi}{d\hat{r}}|$, across the slurry for layer thicknesses of 150 (dashed, blue fill) and 400 km (solid). Control parameters are $Q^s = 2.5$ TW, $Q^{sl} = 5.0$ TW and $k = 100$ Wm⁻¹K⁻¹ (colour online).

572 be evaluated analytically by assuming Stokes' flow and writing

$$\lim_{\hat{r} \rightarrow 1} \left(\frac{d\phi}{d\hat{r}} \right) = \lim_{\hat{r} \rightarrow 1} \left(-\frac{3}{5} \left(\frac{\rho^s v_f}{K_\phi} \right)^{\frac{3}{5}} (-\hat{j})^{-\frac{2}{5}} \frac{d\hat{j}}{d\hat{r}} \right) = -\infty$$

573 On a physical basis Stokes' flow is unlikely to hold in the turbulent mixing
574 region close to the CSB, and the contributions from the variations in ϕ in this
575 thin region are considered to be a numerical artefact of maintaining $\hat{j}(1) = 0$.
576 This thin region comprises less than 5% of the layer and has a limited impact
577 on assessing the overall stability of the slurry.

578 Appendix C. CMB heat flow, Q^c

579 In general contributions to the CMB heat flux can be separated into the
580 secular cooling, Q_s , gravitational power, Q_g , and the latent heat Q_l , while
581 pressure freezing is neglected and radiogenic heating is ignored for the sake of

582 simplicity [24]. This gives a core heat balance of

$$Q^c = Q_s^l + Q_g^l + Q^{sl}, \quad (\text{C.1})$$

583 where

$$Q_s^l = -\frac{c_p}{T_c} \frac{dT_c}{dt} \int_{V^l} \rho T_a \, dV^l \quad (\text{C.2})$$

584 is the secular cooling in the liquid volume, V^l , and

$$Q_g^l = \int_{V^l} \rho \psi \alpha_\xi \frac{d\xi}{dt} \, dV^l - 4\pi (r^{sl})^2 \rho^{sl} \psi^{sl} \alpha_\xi \xi^{sl} v \quad (\text{C.3})$$

585 is the gravitational power in the liquid volume, and Q^{sl} is the heat flux imposed
 586 at the CSB that also contains Q_l . In (C.2), the adiabatic temperature is given
 587 by [23]

$$T_a(r) = T^{sl} \exp\left(-\int_{r^{sl}}^r \frac{g\gamma}{\phi} \, dr\right). \quad (\text{C.4})$$

588 We calculate the core cooling rate, dT_c/dt , by constructing an adiabat anchored
 589 at the present day CSB temperature, followed by constructing a new adiabat
 590 anchored at a new CSB temperature after time Δt due to the advancing layer,
 591 and then finding the resulting decrease in the CMB temperature, $T_c = T_a(r_c)$.
 592 This is given by

$$\frac{dT_c}{dt} \approx \frac{\Delta T_c}{\Delta t} = \frac{T^{sl}(r^{sl} + v\Delta t) \exp\left(-\int_{r^{sl} + v\Delta t}^{r_c} \frac{g\gamma}{\phi} \, dr\right) - T^{sl}(r^{sl}) \exp\left(-\int_{r^{sl}}^{r_c} \frac{g\gamma}{\phi} \, dr\right)}{\Delta t}.$$

593 The gravitational power (C.3), is composed of two parts: the first part is pro-
 594 portional to the change in oxygen concentration in the bulk of the volume, V^l ,
 595 and the second part is from the motion of the CSB, where there is no additional

596 contribution from the motion of the ICB since the CSB and ICB move at the
 597 same rate. By mass conservation, the change in oxygen concentration in the
 598 bulk is given by

$$\int_{V^l} \frac{\partial \xi}{\partial t} dV^l = \frac{-4\pi(r^{sl})^2 \rho^{sl} \xi^{sl} v}{M_l},$$

599 where $M_l = \int_{V^l} \rho dV^l$ is the mass of the liquid outer core.

600 **Appendix D. Definition of the solid expansion coefficient, α_ϕ**

601 The coefficient, α_ϕ , is a dimensionless expansion coefficient that influences
 602 the contribution of the solid fraction to the slurry density. From equation (A3)
 603 of W18, we have that

$$\alpha_\phi \equiv -\rho^{sl} \left(\frac{\partial V}{\partial \phi} \right)_{p,T,\xi}. \quad (\text{D.1})$$

604 From (A1) of W18, the expression for the Gibbs free energy, $d\Phi$, defines the
 605 specific volume as

$$V \equiv \left(\frac{\partial \Phi}{\partial p} \right)_{T,\xi,\phi}. \quad (\text{D.2})$$

606 The lever rule in equation (A9) of W18 gives

$$\left(\frac{\partial \Phi}{\partial \phi} \right)_{p,T,\xi} = \Phi^s - \Phi^l \quad (\text{D.3})$$

607 and

$$\left(\frac{\partial \Phi^s}{\partial p} \right)_{T,\xi,\phi} = V_{Fe}^s, \quad \left(\frac{\partial \Phi^l}{\partial p} \right)_{T,\xi,\phi} = V_{Fe,O}^l, \quad (\text{D.4})$$

608 where Φ^s is the solid part of the Gibbs free energy and Φ^l is the liquid part.

609 Substituting (D.2), (D.3) and (D.4) into (D.1) gives the final result

$$\alpha_\phi = -\rho^{sl} (V_{Fe}^s - V_{Fe,O}^l) = \rho^{sl} \Delta V_{Fe,O}^{s,l}. \quad (\text{D.5})$$

610 References

611 [1] C. M. Hardy, J. Wong, Stably stratified layers within Earth’s core, *Astron-*
612 *omy & Geophysics* 60 (3) (2019) 3–30.

613 [2] A. Dziewonski, D. Anderson, Preliminary Reference Earth Model, *Phys.*
614 *Earth Planet. Int.* 25 (1981) 297–356.

615 [3] A. Souriau, G. Poupinet, The velocity profile at the base of the liquid core
616 from PKP(BC+Cdiff) data: an argument in favor of radial inhomogeneity,
617 *Geophys. Res. Lett.* 18 (1991) 2023–2026.

618 [4] T. Ohtaki, S. Kaneshima, Independent estimate of velocity structure of
619 Earth’s lowermost outer core beneath the northeast Pacific from PKiKP–
620 PKPbc differential travelttime and dispersion in PKPbc, *Journal of Geo-*
621 *physical Research: Solid Earth* 120 (11) (2015) 7572–7586.

622 [5] Z. Zou, K. Koper, V. Cormier, The structure of the base of the outer core
623 inferred from seismic waves diffracted around the inner core, *J. Geophys.*
624 *Res.* 113 (2008) B05314.

625 [6] R. Deguen, Structure and dynamics of Earth’s inner core, *Earth Planet.*
626 *Sci. Lett.* 333–334 (2012) 211–225.

627 [7] F. Nimmo, Energetics of the core, in: G. Schubert (Ed.), *Treatise on Geo-*
628 *physics* 2nd Edn, Vol. 9, Elsevier, Amsterdam, 2015, pp. 31–65.

- 629 [8] T. Alboussière, R. Deguen, Asymmetric dynamics of the inner core and
630 impact on the outer core, *J. Geodyn.* 61 (2012) 172–182.
- 631 [9] D. Gubbins, G. Masters, F. Nimmo, A thermochemical boundary layer at
632 the base of Earth’s outer core and independent estimate of core heat flux,
633 *Geophys. J. Int.* 174 (2008) 1007–1018.
- 634 [10] D. Loper, P. Roberts, On the motion of an iron-alloy core containing a
635 slurry: I. General theory, *Geophys. Astrophys. Fluid Dyn.* 9 (1977) 289–
636 321.
- 637 [11] J. Wong, C. J. Davies, C. A. Jones, A Boussinesq slurry model of the F–
638 layer at the base of Earth’s outer core, *Geophysical Journal International*.
- 639 [12] N. de Koker, G. Steinle-Neumann, V. Vojtech, Electrical resistivity and
640 thermal conductivity of liquid Fe alloys at high P and T and heat flux in
641 Earth’s core, *Proc. Natl. Acad. Sci.* 109 (2012) 4070–4073.
- 642 [13] M. Pozzo, C. Davies, D. Gubbins, D. Alfè, Thermal and electrical conduc-
643 tivity of iron at Earth’s core conditions, *Nature* 485 (2012) 355–358.
- 644 [14] M. Pozzo, C. Davies, D. Gubbins, D. Alfè, Thermal and electrical con-
645 ductivity of solid iron and iron-silicon mixtures at Earth’s core conditions,
646 *Earth Planet. Sci. Lett.* 393 (2014) 159–164.
- 647 [15] R. Deguen, T. Alboussière, S. Labrosse, Double-diffusive translation of
648 Earth’s inner core, *Geophysical Journal International* 214 (1) (2018) 88–
649 107.
- 650 [16] D. Loper, P. Roberts, A Boussinesq model of a slurry, *Structure and Dy-*
651 *namics of Partially Solidified Systems* (1987) 291–323.
- 652 [17] F. Birch, Elasticity and the constitution of Earth’s interior, *J. Geophys.*
653 *Res.* 66 (1952) 227–286.

- 654 [18] D. Alfè, M. Gillan, G. Price, Composition and temperature of the Earth's
655 core constrained by combining *ab initio* calculations and seismic data,
656 Earth Planet. Sci. Lett. 195 (2002) 91–98.
- 657 [19] J. Badro, A. Côté, J. Brodholt, A seismologically consistent compositional
658 model of Earth's core, Proc. Natl. Acad. Sci. 111 (2014) 7542–7545.
- 659 [20] H. Gomi, K. Ohta, K. Hirose, S. Labrosse, R. Caracas, V. Verstraete,
660 J. Hernlund, The high conductivity of iron and thermal evolution of the
661 Earth's core, Phys. Earth Planet. Int. 224 (2013) 88–103.
- 662 [21] Q. Williams, The thermal conductivity of Earth's core: A key geophysical
663 parameter's constraints and uncertainties, Annual Review of Earth and
664 Planetary Sciences 46 (1).
- 665 [22] R. Deguen, T. Alboussière, D. Brito, On the existence and structure of a
666 mush at the inner core boundary of the Earth, Phys. Earth Planet. Int. 164
667 (2007) 36–49.
- 668 [23] D. Gubbins, D. Alfe, G. Masters, G. Price, M. Gillan, Can the Earth's
669 dynamo run on heat alone?, Geophys. J. Int. 155 (2003) 609–622.
- 670 [24] D. Gubbins, D. Alfè, G. Masters, G. Price, M. Gillan, Gross thermodynam-
671 ics of two-component core convection, Geophys. J. Int. 157 (2004) 1407–
672 1414.
- 673 [25] M. Pozzo, C. Davies, D. Gubbins, D. Alfè, Transport properties for liquid
674 silicon-oxygen-iron mixtures at Earth's core conditions, Phys. Rev. B 87
675 (2013) 014110.
- 676 [26] C. Davies, Cooling history of Earth's core with high thermal conductivity,
677 Phys. Earth Planet. Int.

- 678 [27] C. Davies, M. Pozzo, D. Gubbins, D. Alfè, Constraints from material prop-
679 erties on the dynamics and evolution of Earth’s core, *Nat. Geosci.* 8 (2015)
680 678–687.
- 681 [28] P. Virtanen, R. Gommers, T. Oliphant, M. Haberland, T. Reddy, D. Cour-
682 napeau, E. Burovski, P. Peterson, W. Weckesser, J. Bright, et al., *Scipy*
683 1.0: fundamental algorithms for scientific computing in Python, *Nature*
684 *methods* 17 (3) (2020) 261–272.
- 685 [29] J. Wong, *nondim-slurry_v0.1*, (2021), doi:10.5281/zenodo.4446750.
- 686 [30] T. Lay, J. Hernlund, B. Buffett, Core-mantle boundary heat flow, *Nat.*
687 *Geosci.* 1 (2008) 25–32.
- 688 [31] F. Stacey, D. Loper, A revised estimate of the conductivity of iron alloy
689 at high pressure and implications for the core energy balance, *Phys. Earth*
690 *Planet. Int.* 161 (2007) 13–18.
- 691 [32] K. Hirose, S. Labrosse, J. Hernlund, Compositional state of Earth’s core,
692 *Annual Review of Earth and Planetary Sciences* 41 (2013) 657–691.
- 693 [33] R. Sinmyo, K. Hirose, Y. Ohishi, Melting curve of iron to 290 GPa de-
694 termined in a resistance-heated diamond-anvil cell, *Earth and Planetary*
695 *Science Letters* 510 (2019) 45–52.
- 696 [34] J. Jackson, W. Sturhahn, M. Lerche, J. Zhao, T. Toellner, E. Ercan Alp,
697 S. Sinogeikin, J. Bass, C. Murphy, J. Wicks, Melting of compressed iron by
698 monitoring atomic dynamics, *Earth Planet. Sci. Lett.* 362 (2013) 143–150.
- 699 [35] G. Masters, D. Gubbins, On the resolution of density within the Earth,
700 *Phys. Earth Planet. Int.* 140 (2003) 159–167.

- 701 [36] K. D. Koper, M. Dombrovskaya, Seismic properties of the inner core bound-
702 ary from PKiKP/P amplitude ratios, *Earth Planet. Sci. Lett.* 237 (2005)
703 680–694.
- 704 [37] H. Tkalčić, B. Kennett, V. Cormier, On the inner–outer core density con-
705 trast from PKiKP/PcP amplitude ratios and uncertainties caused by seis-
706 mic noise, *Geophys. J. Int.* 179 (2009) 425–443.
- 707 [38] D. Loper, P. Roberts, On the motion of an iron-alloy core containing a
708 slurry: II. A simple model, *Geophys. Astrophys. Fluid Dyn.* 16 (1980) 83–
709 127.
- 710 [39] V. Solomatov, Magma oceans and primordial mantle differentiation., in:
711 G. Schubert, B. Romanowicz, A. Dziewonski (Eds.), *Treatise on geophysics*,
712 Elsevier, Amsterdam, 2015, pp. 655–693.
- 713 [40] S. Cottaar, T. Heister, I. Rose, C. Unterborn, Burnman: A lower man-
714 tle mineral physics toolkit, *Geochemistry, Geophysics, Geosystems* 15 (4)
715 (2014) 1164–1179.
- 716 [41] B. Kennett, E. Engdahl, R. Buland, Constraints on seismic velocities in
717 the Earth from traveltimes, *Geophys. J. Int.* 122 (1995) 108–124.
- 718 [42] S. Labrosse, Thermal and compositional stratification of the inner core, *C.*
719 *R. Geosci.* 346 (2014) 119–129.
- 720 [43] L. Huguet, J. Van Orman, S. Hauck II, M. Willard, Earth’s inner core
721 nucleation paradox, *Earth Planet. Sci. Lett.* 487 (2018) 9–20.
- 722 [44] C. J. Davies, M. Pozzo, D. Alfè, Assessing the inner core nucleation paradox
723 with atomic-scale simulations, *Earth and Planetary Science Letters* 507
724 (2019) 1–9.

- 725 [45] M. Lasbleis, M. Kervazo, G. Choblet, The fate of liquids trapped during
726 the Earth's inner core growth, arXiv preprint arXiv:1912.12258.
- 727 [46] M. Bouffard, M. Landeau, A. Goument, Convective erosion of a primordial
728 stratification atop Earth's core, *Geophysical Research Letters*.
- 729 [47] J. Wong, A slurry model of the F-layer in the Earth's core, Ph.D. thesis,
730 University of Leeds (2018).
- 731 [48] J. D. Hunter, Matplotlib: A 2D graphics environment, *Computing in Sci-*
732 *ence & Engineering* 9 (3) (2007) 90–95. doi:10.1109/MCSE.2007.55.

Declaration of interests

The authors declare that they have no known competing financial interests or personal relationships that could have appeared to influence the work reported in this paper.

The authors declare the following financial interests/personal relationships which may be considered as potential competing interests:

Jenny Wong: Conceptualisation, Methodology, Investigation, Writing – Original Draft,
Writing - Review & Editing

Christopher J. Davies: Conceptualisation, Writing - Review & Editing, Supervision

Christopher A. Jones: Writing - Review & Editing